

# Bioinspired CNNs for border completion in occluded images

Catarina P. Coutinho<sup>1</sup>[0000-0003-3707-8795], Aneeqa Merhab<sup>2</sup>[0009-0004-8013-3061], Janko Petkovic<sup>3</sup>[0009-0009-7455-9484], Ferdinando Zanchetta<sup>1</sup>[0000-0003-2294-2755], and Rita Fioresi<sup>1</sup>[0000-0003-4075-7641]

<sup>1</sup> Department of Pharmacy and Biotechnology, University of Bologna, Via San Donato 15, 40127 Bologna, Italy [catarina.praefke2@unibo.it](mailto:catarina.praefke2@unibo.it), [rita.fioresi@unibo.it](mailto:rita.fioresi@unibo.it), [ferdinando.zanchett2@unibo.it](mailto:ferdinando.zanchett2@unibo.it)

<sup>2</sup> Department of Mathematics, University of Ferrara, Via Ariosto 35, 44122 Ferrara, Italy [aneeqa.mehrab@unife.it](mailto:aneeqa.mehrab@unife.it)

<sup>3</sup> Numerical Analysis and Applied Mathematics, VIB - KU Leuven, ON5/B Herestraat 49 - Bus 4039, 3000 Leuven, Belgium [janko.petkovic@kuleuven.be](mailto:janko.petkovic@kuleuven.be)

**Abstract.** We exploit the mathematical modeling of the border completion problem in the visual cortex to design convolutional neural network (CNN) filters that enhance robustness to image occlusions. We evaluate our CNN architecture, BorderNet, on three occluded datasets MNIST, Fashion-MNIST, and EMNIST under two types of occlusions: stripes and grids. In all cases, BorderNet demonstrates improved performance, with gains varying depending on the severity of the occlusions and the dataset.

**Keywords:** Convolutional Neural Networks · Visual Cortex · Border completion · Occlusions

## 1 Introduction

Visual encoding of information in higher mammals faces significant challenges, as for example, situations where occlusions partially hide an object, making its identification nontrivial. The mathematical modelling of mammalian visual cortex (V1) ability to reconstruct partially occluded images, is a current and active research area (see [6] and refs. therein). Starting from the pioneering study by Hubel and Wiesel, [14, 15], whose ice-cube model of the visual cortex first provided a functionally meaningful anatomic characterization of the primary visual cortex, later models focused in understanding finer mechanisms as in [13], where Hoffman provides a mathematical representation of V1 as a contact bundle, explaining the orientation selectivity occurring in contour detection. In fact, anatomically, the border directions in a perceived image are selected within hypercolumns, the functional units in V1 composed of columns of neurons tuned to specific orientations. Each column responds maximally to a preferred orientation, enabling the construction of a local orientation map across the visual field. Information from the dominant orientation at each location is then relayed to higher cortical areas for further processing [10]. A key functional property

emerging from this hypercolumnar organization is *contour integration*, which is the ability to reconstruct partially occluded boundaries from their visible portions. This phenomenon was first described on a phenomenological level by Gestalt psychology under the law of good continuation, one of the Prägnanz principles governing perceptual organization [16]. Continuity plays a central role in shape perception, allowing the visual system to integrate spatially distributed orientation cues into smooth and coherent contours. Neurophysiologically, this capability is supported by the horizontal connectivity between hypercolumns: neurons with collinear orientation preferences tend to excite each other, while orthogonally tuned neurons are inhibited. These association fields as in Figure 1, [10] effectively promote the completion of interrupted contours, providing a biological solution to the occlusion problem.

This understanding of receptive fields of simple and complex cells, together with the anatomically observed structured arrangement of the orientation selective columns, led to finer mathematical formulations grounded in differential geometry (see [3], [4], [18], [5], [2]). In particular, modeling V1 as a contact bundle as in [13] led to take advantage of the natural sub-Riemannian structure thus providing a rigorous framework in which contour completion can be interpreted as the solution of a sub-Riemannian geodesic problem. At the same time a growing number of researchers in machine learning, started to draw a closer parallelism between the human visual perception and the successful algorithms of deep learning (see [12], [9], [8] and refs. therein).

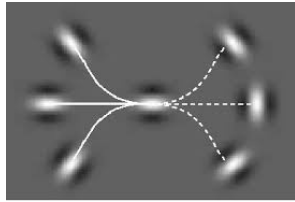


Fig. 1: Association Fields

In this work, we want to present the border completion in V1 from a theoretical point of view, via the Hamiltonian sub Riemannian formalism along the lines in [11], which however had a different scope. Then, we shall take advantage of the mathematical modelling to investigate how the biological mechanisms underlying contour integration can be translated into a computational framework to enhance convolutional neural networks (CNNs) robustness against occlusions in image classification tasks. Building on our previous geometric models of V1, we introduce biologically inspired directional filters into LeNet5, a CNN whose architecture bears notable similarities to the early visual pathway [19]. These predefined filters mimic the action of orientation-selective receptive fields and border integration operators.

We test our proposed architecture BorderNet on occluded versions of the MNIST, FashionMNIST and EMNIST datasets, where images are corrupted by diagonal black stripes, and grids. Our model is trained exclusively on the original, unmodified dataset; occluded images are used only at test time. Our results show that incorporating orientation-aware filters significantly improves classification accuracy under such occlusions, thus confirming the proof of concept preliminary results obtained in [7].

This paper is organized as follows.

Section 2 reviews the mathematical framework underlying our approach and details the proposed bio-inspired architecture and dataset construction.

Sections 3 and 4 present and discuss the experimental results, comparing the performance of the standard LeNet5 model with that of the enhanced network endowed with border integration capabilities.

## 2 Mathematical Modeling for border completion in V1

In this section we discuss the mathematical modeling for the mechanism of border completion in the primary visual cortex V1, via the calculation of the sub Riemannian geodesics with respect to a bracket generating distribution. We shall use the Hamiltonian formalism, instead of the more established Lagrangian one [5], [18]. These calculations appeared originally in [11]; we briefly recap them, since the different focus and scope of [11] may not make the reader aware of their significance for the present purpose.

In sub Riemannian geometry, the metric on a manifold  $M$  is replaced by a sub Riemannian metric, which is a semidefinite positive symmetric bilinear form  $g$  on the tangent bundle, typically assumed to be of constant (non maximal) rank (see [1], [17] and refs. therein). Hence its non degenerate locus defines a distribution  $\mathcal{D}$  on  $M$ , i.e. a smooth assignment

$$M \ni x \mapsto \mathcal{D}_x \subset T_x M, \quad g|_{\mathcal{D}_x} \text{ non degenerate}, \quad (1)$$

where  $\dim \mathcal{D}_x < \dim T_x M$ . We call a distribution *bracket generating*

when a finite number of brackets of the vector fields that generate it, generate the tangent space to  $M$  at each point. Typically (but not always) in sub Riemannian geometry we assume the distribution  $\mathcal{D}$  as in (1) to be bracket generating. We call *sub Riemannian geodesics* for the sub Riemannian metric  $g$  the shortest paths connecting two given points in the manifold  $M$ . In general, the sub Riemannian geodesic problem may not have a solution and when the solution exists it may not be unique: the Hamiltonian or Lagrangian formulation of the question may indeed lead to different solutions [17]. However, despite the fact the two approaches are not in general equivalent in sub Riemannian geometry, with some extra regularity hypotheses, as for example the assumption of  $\mathcal{D}$  coming from a principal bundle distribution, they are. We will see that indeed, viewing the visual cortex as contact bundle as in [13], gives to it a natural a principal bundle structure [2], so that the Hamiltonian and Lagrangian formulations for the geodesic question lead to the same answer.

We start by modeling the functional architecture of the primary visual cortex in its border completion capability, (see [18], [5], [6] and refs therein). We represent an image by a smooth function  $I : D \subset \mathbb{R}^2 \rightarrow \mathbb{R}$ , each point  $(x, y) \in D$  with  $I(x, y)$  giving its grey level.

We define the vector field  $Z$  on the manifold  $\mathcal{E} = \mathbb{R}^2 \times S^1$  with coordinates  $(x, y, \theta)$ :

$$Z = -\sin \theta \partial_x + \cos \theta \partial_y.$$

where  $(x, y)$  are the coordinate of a point in  $\mathbb{R}^2$  and  $\theta$  represents an angle.

The vector field  $Z$  is orthogonal to the line with angle  $\theta$  with the  $x$ -axis at each point.

Motivated by the action of orientation-selective cells, in the visual cortex, following [19], [11], we give a key definition.

**Definition 1.** Let  $\text{reg}(D)$  be the set of points where  $\nabla I \neq 0$ . The *orientation map* of  $I$  is

$$\Theta(x, y) = \operatorname{argmax}_{\theta \in S^1} \{Z(\theta)I(x, y)\}, \quad (x, y) \in \text{reg}(D).$$

Since  $Z(\theta)I = -\sin \theta \partial_x I + \cos \theta \partial_y I$  the above maximization selects the direction for which  $Z(\theta)$  aligns with  $\nabla I$ . Hence  $\Theta$  assigns to each point the orientation orthogonal to the image level set  $I(x, y) = \text{constant}$ , passing through it. We may think of such image level set as the contour of an object depicted by the image represented by  $I$ .

To describe border completion, we introduce the horizontal distribution on  $\mathcal{E}$ :

$$\mathcal{D} = \text{span}\{X, Y\}, \quad X = \partial_\theta, \quad Y = \cos \theta \partial_x + \sin \theta \partial_y.$$

The word "horizontal" refers to the fact that this distribution is orthogonal to the vector field  $Z = [X, Y]$  with respect to the euclidean metric. The fact that the bracket  $[X, Y] = Z$  shows that  $\mathcal{D}$  is indeed bracket generating: this guarantees the solution of the geodesic existence question (Chow's Thm, see [17]).

Notice that  $\mathcal{E} \cong \text{SE}(2)$  the special euclidean group, semidirect product of translations  $\mathbb{R}^2$  and rotations  $S^1$ . Notice furtherly that  $\mathcal{E} \rightarrow \mathcal{E}/S^1 \cong \mathbb{R}^2$  is a  $S^1$  principal bundle. Endowing  $\mathcal{D}$  with the natural invariant metric makes  $(\mathcal{E}, \mathcal{D})$  a sub-Riemannian manifold, invariant under the action of  $\text{SE}(2) \cong \mathcal{E}$  the special euclidean group.

This fact makes the solution to the sub Riemannian geodesic problem unique.

Horizontal curves, i.e. curves tangent to the distribution  $\mathcal{D}$  are  $\Sigma(t) = (x(t), y(t), \theta(t))$  satisfying

$$\dot{\Sigma} = u_1 X + u_2 Y,$$

They represent admissible transitions of position and orientation. Geodesics minimize their sub-Riemannian length, or equivalently, in the Hamiltonian formalism, the Hamiltonian

$$H = \frac{1}{2}(P_X^2 + P_Y^2),$$

where

$$P_X = \cos \theta p_x + \sin \theta p_y, \quad P_Y = p_\theta.$$

In local coordinates the Hamiltonian reads

$$H = \frac{1}{2}[(\cos \theta p_x + \sin \theta p_y)^2 + p_\theta^2].$$

We now compute the geodesics in the Hamiltonian formulation:

$$\begin{cases} \dot{x} = \cos \theta p_1, \\ \dot{y} = \sin \theta p_1, \\ \dot{\theta} = p_2, \end{cases} \quad \begin{cases} \dot{p}_1 = p_2 p_3, \\ \dot{p}_2 = -p_1 p_3, \\ \dot{p}_3 = -p_1 p_2, \end{cases}$$

where

$$p_1 = P_X, \quad p_2 = P_Y, \quad p_3 = -\sin \theta p_x + \cos \theta p_y.$$

Since  $H$  is conserved, let  $E = 2H = p_1^2 + p_2^2$ . Introducing a phase variable  $\gamma(t)$  such that

$$p_1 = \sqrt{E} \sin \frac{\gamma}{2}, \quad p_2 = \sqrt{E} \cos \frac{\gamma}{2}, \quad p_3 = \frac{1}{2} \dot{\gamma},$$

the projected dynamics become

$$\begin{cases} \dot{x} = \sqrt{E} \sin \frac{\gamma}{2} \cos \theta, \\ \dot{y} = \sqrt{E} \sin \frac{\gamma}{2} \sin \theta, \\ \dot{\theta} = \sqrt{E} \cos \frac{\gamma}{2}. \end{cases}$$

Numerical integration provides the geodesics whose projection in the  $x, y$  plane is depicted in Figure 2. They agree with the celebrated Hayes field as in Figure 1.

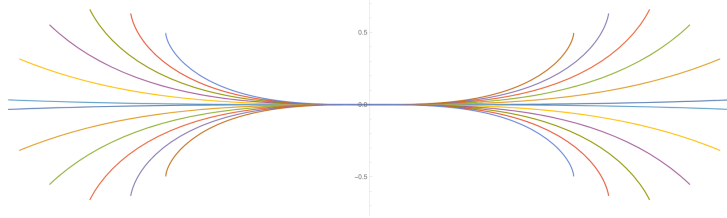


Fig. 2: Numerical solutions of the geodesic equations for some values of  $\gamma$

In the next section we shall exploit the modelling of orientation via the vector field  $Z$  to enhance border completion capabilities of neural networks.

### 3 Experiments

We create a new CNN model in which custom filters are added by mimicking the orientation map (1) in our mathematical modelling.

**CNN models.** We considered two CNN models in our study: the LeNet5 (Vanilla LeNet5) and a modified LeNet5, called BorderNet, in which four custom filters were added at the beginning as a sequence of convolutions: see Figure 3 for

a scheme describing the structure and differences of LeNet5 and BorderNet. The filters of BorderNet were created based on the analogy with the visual cortex, each filter featuring one direction - horizontal, vertical, and both diagonals (see Figure 4). Filters were defined with a size of  $7 \times 7$  pixels and a stripe width of 3 pixels, where the pixels belonging to the oriented stripe were set to the value of 1, while the remaining background was set to 0. In this fashion, a convolution with the filter would mimics the action of the vector field  $Z$  as described above.

**Datasets.** We examine the performance of the two CNN models on three datasets: MNIST, Fashion MNIST and Extended MNIST digits (EMNIST). For each dataset, both models were trained on unoccluded images using the ADAM optimizer, with a learning rate of 0.001, 10 epochs, and a batch size of 64. The testing was carried out using the occluded images. To reduce variability inherent to our models, we performed 100 cycles for each experiment, using a fixed random seed (seed=42) to ensure reproducibility. Individual model accuracies were calculated as the mean over the 100 cycles for each combination of occlusion stripe width and spacing. For model comparison, we computed an accuracy improvement of BorderNet with respect to LeNet5 which does not follow a normal distribution. We therefore chose to express it as the median improvement, associated with 95% confidence intervals bootstrapped with 100000 bootstrap samples.

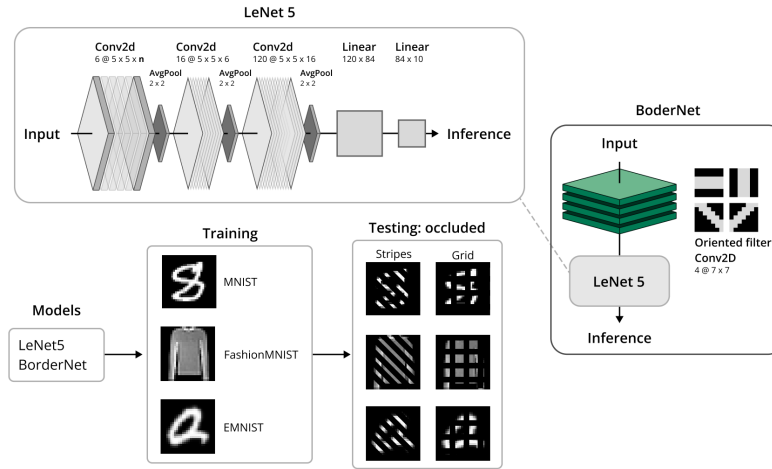


Fig. 3: Implemented pipeline with Vanilla LeNet5 and BorderNet trained on unoccluded images of the three different datasets (MNIST/FashionMNIST/EMNIST) and tested on two types of occluded images (stripes/grid).

**Occlusions in Test Datasets.** To test robustness of our modified LeNet5, i.e. BorderNet, we created test datasets consisting of two types of occluded im-

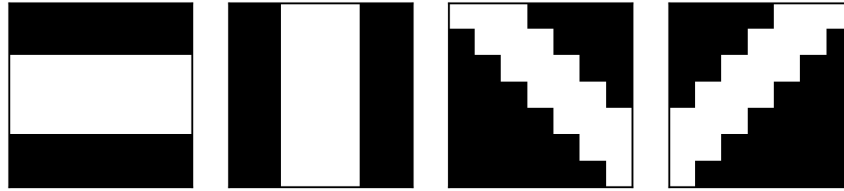


Fig. 4: BorderNet oriented filters.

ages as in Fig. 5. For stripe occlusions we take a masking composed of diagonal straight stripes of width  $w$  and inter-stripe spacing  $s$ , whereas for grid occlusions instead of diagonal stripes we considered square grids composed of horizontal and vertical stripes. To conduct a thorough benchmarking, we test all the models on all the occlusions obtained from the pairwise combination of  $s, w \in [1, 10]$  for each dataset separately (see Figure 3 for a scheme of our pipeline).

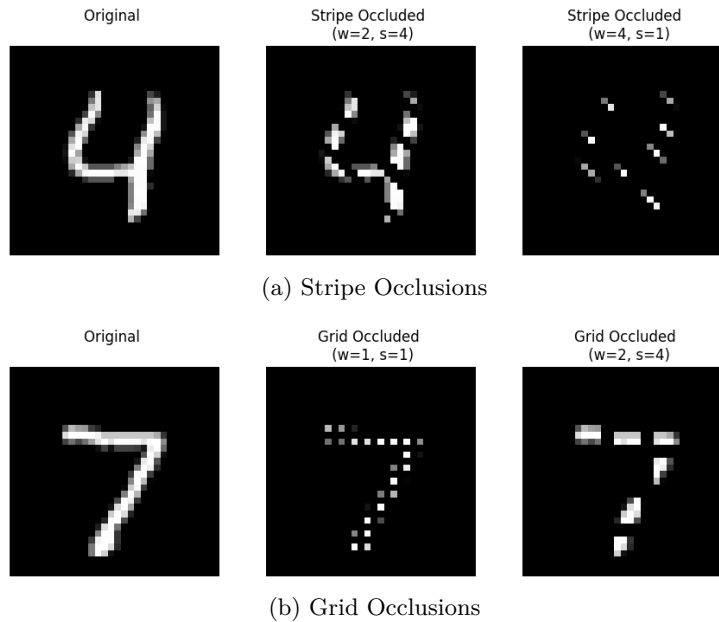


Fig. 5: Sample of images occluded with stripes (top row) and grids (bottom row) used in the testing phase occluded.

## 4 Results

LeNet5 and BorderNet accuracies are reported in this section. Table 1 lists the mean accuracies of our models, separately for the MNIST, FashionMNIST and EMNIST images occluded with stripes. Table 2 reports the same outcomes but for grid occlusions. Bootstrapped median improvement comparison of BorderNet over LeNet5 are also reported.

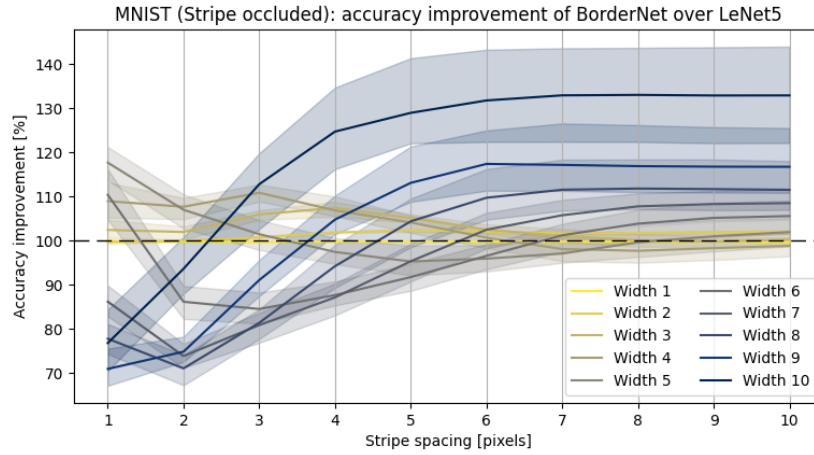
Table 1: Mean Accuracies of Vanilla LeNet5 and BorderNet for some examples of **stripe** occlusions for MNIST/FashionMNIST/EMNIST for different combinations of stripe width and stripe spacing  $(w,s)$ . Improvement (Imp.\*) of BorderNet over Vanilla LeNet5 are the bootstrapped medians in percentage.

$(w,s)$	MNIST			FashionMNIST			EMNIST		
	LeNet5	BorderNet	Imp.*	LeNet5	BorderNet	Imp.*	LeNet5	BorderNet	Imp.*
(1,1)	0.974	0.974	99.90%	0.848	0.853	100.60%	0.989	0.985	99.70%
(1,10)	0.982	0.979	99.70%	0.854	0.867	101.50%	0.991	0.988	99.70%
(2,4)	0.939	0.960	101.80%	0.822	0.774	95.20%	0.962	0.976	101.30%
(3,3)	0.788	0.839	105.90%	0.689	0.683	100.70%	0.843	0.891	105.20%
(4,1)	0.573	0.630	108.90%	0.514	0.523	101.20%	0.673	0.697	103.70%
(5,3)	0.419	0.426	101.40%	0.362	0.375	103.60%	0.412	0.603	147.10%
(6,4)	0.354	0.313	87.60%	0.354	0.385	112.50%	0.322	0.477	147.60%
(7,9)	0.362	0.389	108.30%	0.322	0.268	83.90%	0.446	0.466	105.80%
(8,6)	0.291	0.321	109.70%	0.253	0.230	91.40%	0.338	0.366	109.90%
(9,3)	0.229	0.215	91.00%	0.223	0.212	96.60%	0.224	0.251	112.50%
(10,1)	0.178	0.142	76.70%	0.156	0.206	139.40%	0.167	0.170	100.70%
(10,10)	0.178	0.242	132.90%	0.170	0.309	186.80%	0.282	0.326	119.50%

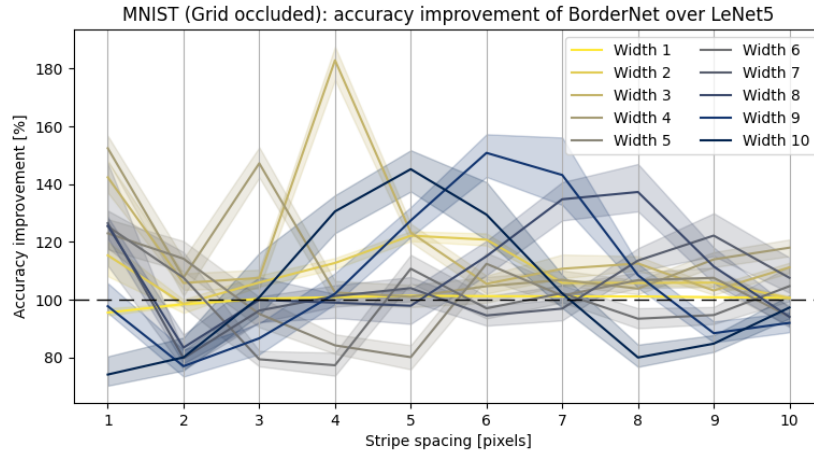
Table 2: Mean Accuracies of Vanilla LeNet5 and BorderNet for some examples of **grid** occlusions for MNIST/FashionMNIST/EMNIST for different combinations of stripe width and stripe spacing  $(w,s)$ . Improvement (Imp.\*) of BorderNet over Vanilla LeNet5 are the bootstrapped medians in percentage.

$(w,s)$	MNIST			FashionMNIST			EMNIST		
	LeNet5	BorderNet	Imp.*	LeNet5	BorderNet	Imp.*	LeNet5	BorderNet	Imp.*
(1,1)	0.882	0.859	95.50%	0.722	0.717	99.60%	0.939	0.890	94.10%
(1,10)	0.966	0.973	106.60%	0.823	0.852	103.40%	0.979	0.984	100.50%
(2,4)	0.674	0.764	112.70%	0.549	0.675	123.30%	0.647	0.811	125.80%
(3,3)	0.384	0.412	107.50%	0.381	0.433	113.40%	0.398	0.413	102.00%
(4,1)	0.153	0.234	152.40%	0.174	0.304	177.50%	0.143	0.168	120.20%
(5,3)	0.211	0.205	95.10%	0.300	0.258	87.80%	0.274	0.292	104.10%
(6,4)	0.250	0.198	77.20%	0.163	0.243	155.90%	0.207	0.219	105.10%
(7,9)	0.232	0.285	122.20%	0.317	0.304	96.60%	0.319	0.351	108.20%
(8,6)	0.182	0.209	115.00%	0.235	0.240	102.60%	0.259	0.258	99.70%
(9,3)	0.158	0.145	86.60%	0.195	0.177	88.90%	0.168	0.158	95.60%
(10,1)	0.117	0.106	74.00%	0.125	0.166	168.00%	0.108	0.110	100.00%
(10,10)	0.372	0.366	97.20%	0.241	0.183	72.10%	0.279	0.225	81.40%

We see a consistent improvement when comparing BorderNet with LeNet5 except in the case of severe occlusions, where no comparison can be significant. We also depict graphically the improvement comparison results for all widths and stripe spacing for the MNIST (Figure 6), FashionMNIST (Figure 7) and EMNIST datasets (Figure 8). Single model’s performance graphs for each type of occlusions can be found in the Supplementary Material.

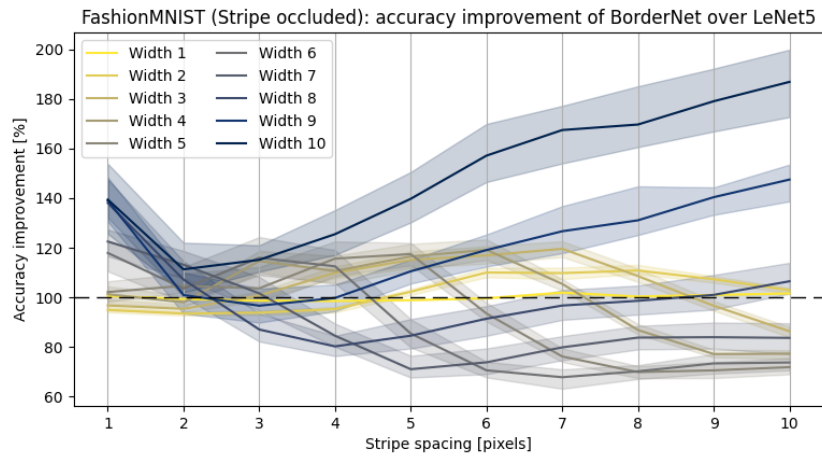


(a) MNIST Stripe Occlusions

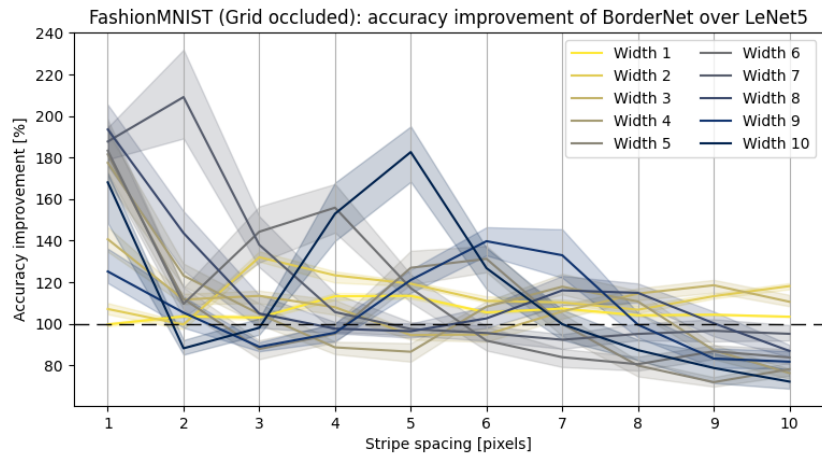


(b) MNIST Grid Occlusions

Fig. 6: Accuracy improvement of BorderNet with respect to Vanilla LeNet5 for occluded MNIST images with stripes (a) and grid (b).

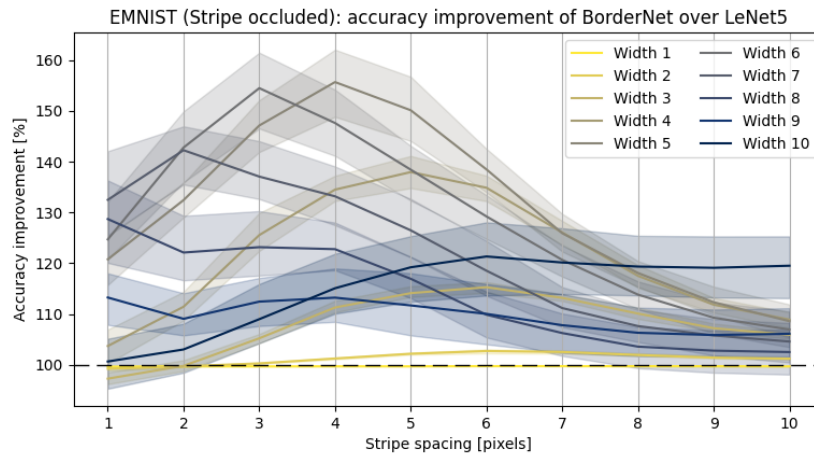


(a) FashionMNIST Stripe Occlusions

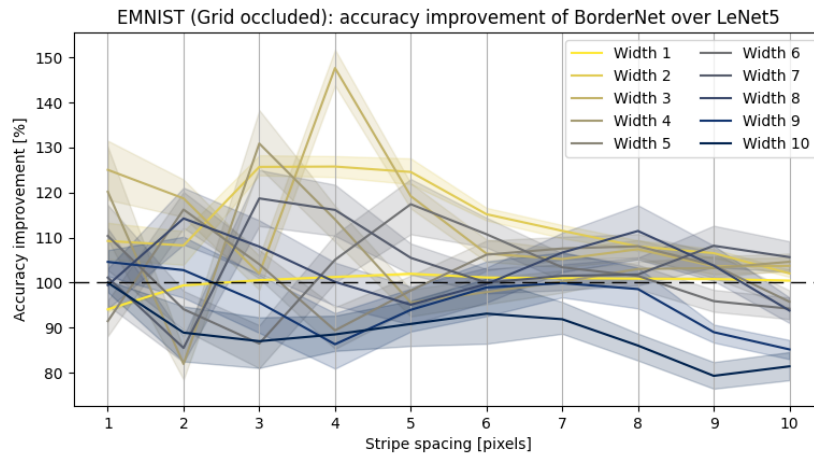


(b) FashionMNIST Grid Occlusions

Fig. 7: Accuracy improvement of BorderNet with respect to Vanilla LeNet5 for occluded FashionMNIST images with stripes (a) and grid (b).



(a) EMNIST Stripe Occlusions



(b) EMNIST Grid Occlusions

Fig. 8: Accuracy improvement of BorderNet with respect to Vanilla LeNet5 for occluded EMNIST images with stripes (a) and grid (b).

## 5 Conclusions

We show how BorderNet, a CNN model with bioinspired filters, performs consistently better than LeNet5 on occluded test images from three different datasets: MNIST, FashionMNIST and EMNIST and with respect to two diverse sets of occlusions, stripes and grids. This confirms the proof of concept result expressed in [7] and suggest future directions in bioinspired CNNs.

**Acknowledgments.** We thank Prof. R. Duits for helpful comments and observations regarding our work.

The research of the first author was supported by a research scholarship funded by the European Union-Next Generation EU, Missione 4 Component 1 CUP J33C24001310009. This research was funded by CaLISTA CA 21109, CaLIGOLA MSCA-2021-SE-01-101086123, MSCA-DN CaLiForNIA101119552, PNRR MNESYS, the PNRR National Center for HPC, Big Data, and Quantum Computing, SimQuSec; INFN Sezione Bologna, Gast initiative and GNSAGA Indam.

**Disclosure of Interests.** The authors have no competing interests.

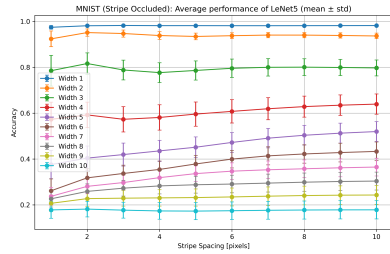
## References

1. Agrachev, A.A., Barilari, D., Boscain, U.V.: A comprehensive introduction to subriemannian geometry (2019)
2. Alekseevsky, D.V., Spiro, A.F.: Conformal models for hypercolumns and the visual v1 cortex. <https://arxiv.org/abs/2202.10157> (2022)
3. Bressloff, P., Cowan, J.: The functional geometry of local and horizontal connections in a model of v1. *Journal of physiology, Paris* **97**, 221–36 (03 2003). <https://doi.org/10.1016/j.jphysparis.2003.09.017>
4. Bressloff, P.C., Cowan, J.D.: The visual cortex as a crystal. *Physica D: Nonlinear Phenomena* **173**, 226–258 (2002)
5. Citti, G., Sarti, A.: A cortical based model of perceptual completion in the roto-translation space. *J Math Imaging* **24**, 307–326 (2006)
6. Citti, G., Sarti, A.: *Neuromathematics of vision* (2014)
7. Coutinho, C.P., Merhab, A., Petkovic, J., Zanchetta, F., Fioresi, R.: Enhancing cnns robustness to occlusions with bioinspired filters for border completion. In: *International Conference on Geometric Science of Information* (2025)
8. Duits, R., Franken, E.: Left-invariant parabolic evolutions on  $se(2)$  and contour enhancement via invertible orientation scores. part i: Linear left-invariant diffusion equations on  $se(2)$ . *Quarterly of Applied Mathematics* **68**, 255–292 (2010)
9. Ecker, A.S., Sinz, F.H., Froudarakis, E., Fahey, P.G., Cadena, S.A., Walker, E.Y., Cobos, E., Reimer, J., Tolias, A.S., Bethge, M.: A rotation-equivariant convolutional neural network model of primary visual cortex. *ArXiv* **abs/1809.10504** (2018)
10. Field, D.J., Hayes, A., Hess, R.F.: Contour integration by the human visual system: Evidence for a local association field. *Vision Research* **33**(2), 173–193 (1993)
11. Fioresi, R., Marraffa, A., Petkovic, J.: A new perspective on border completion in visual cortex as bicycle rear wheel geodesics paths via sub riemannian hamiltonian formalism. *Differential Geometry and its Applications* (2023), <https://api.semanticscholar.org/CorpusID:257912491>

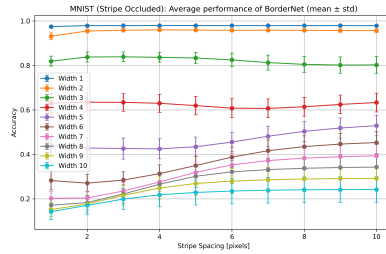
12. Fukushima, K.: Neocognitron: A self-organizing neural network model for a mechanism of pattern recognition unaffected by shift in position. *Biological Cybernetics* **36**, 193–202 (1980)
13. Hoffman, W.C.: The visual cortex is a contact bundle. *Applied Mathematics and Computation* **32**, 137–167 (1989)
14. Hubel, D.H., Wiesel, T.N.: Anatomical demonstration of columns in the monkey striate cortex. *Nature* **221**, 747–750 (1969)
15. Hubel, D.H., Wiesel, T.N.: Uniformity of monkey striate cortex: A parallel relationship between field size, scatter, and magnification factor. *Journal of Comparative Neurology* **158** (1974)
16. Mather, G.: *Foundations of perception* (2006)
17. Montgomery, R.: *A tour of subriemannian geometries, their geodesics and applications* (2006)
18. Petitot, J., Tondut, Y.: *Vers une neurogéométrie. fibrations corticales, structures de contact et contours subjectifs modaux* (1999)
19. Petkovic, J., Fioresi, R.: Spontaneous emergence of robustness to light variation in cnns with a precortically inspired module. *Neural Computation* **36**, 1832–1853 (2024), <https://api.semanticscholar.org/CorpusID:271744564>

## Supplementary Material

For each dataset (MNIST/FashionMNIST/EMNIST) and occlusion type (grid/stripe) plots of mean accuracies and standard deviation for Vanilla LeNet5 and BorderNet are presented.

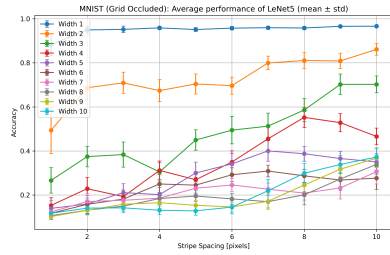


(a) Vanilla LeNet5

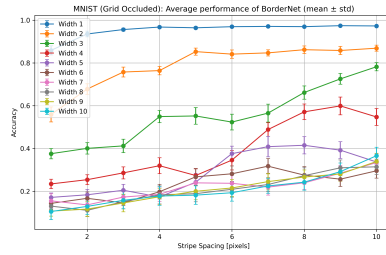


(b) BorderNet

Fig. 9: Accuracies with MNIST occlusion stripe spacing and width for the Vanilla LeNet5 and BorderNet.

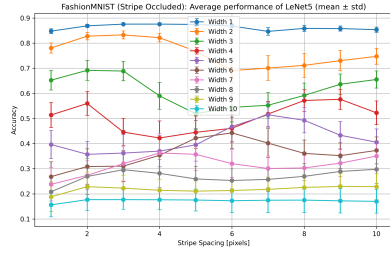


(a) Vanilla LeNet5

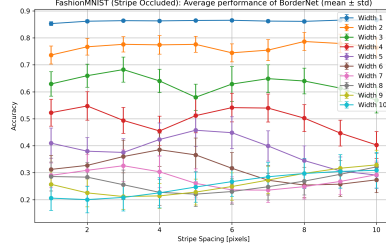


(b) BorderNet

Fig. 10: Accuracies with MNIST occlusion grid spacing and width for the Vanilla LeNet5 and BorderNet.

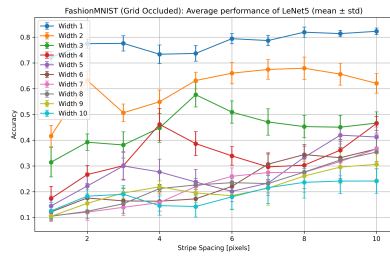


(a) Vanilla LeNet5

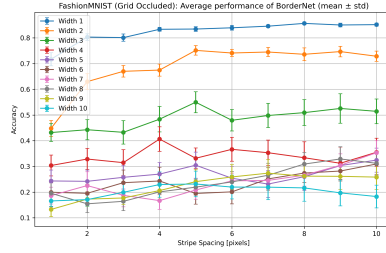


(b) BorderNet

Fig. 11: Accuracies with FashionMNIST occlusion stripe spacing and width for the Vanilla LeNet5 and BorderNet.

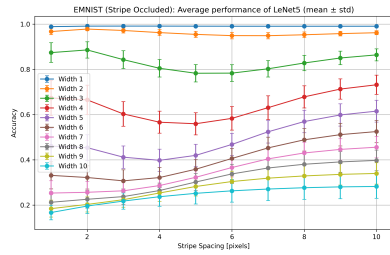


(a) Vanilla LeNet5

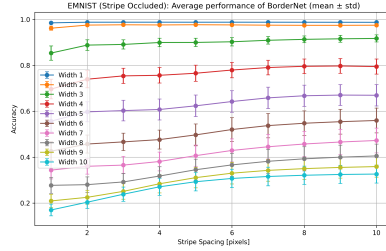


(b) BorderNet

Fig. 12: Accuracies with FashionMNIST occlusion grid spacing and width for the Vanilla LeNet5 and BorderNet.

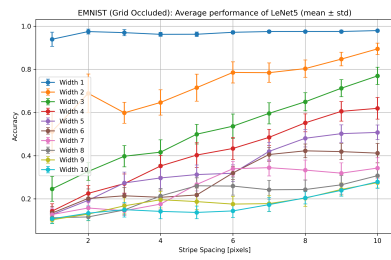


(a) Vanilla LeNet5

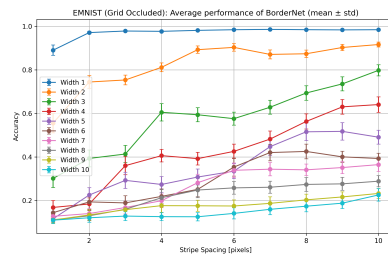


(b) BorderNet

Fig. 13: Accuracies with EMNIST occlusion stripe spacing and width for the Vanilla LeNet5 and BorderNet.



(a) Vanilla LeNet5



(b) BorderNet

Fig. 14: Accuracies with EMNIST occlusion grid spacing and width for the Vanilla LeNet5 and BorderNet.